Development of an Operational Convective Nowcasting Algorithm Using Raindrop Size Sorting Information from Polarimetric Radar Data

DARREL M. KINGFIELD[a]

Cooperative Institute for Mesoscale Meteorological Studies, University of Oklahoma, and NOAA/OAR/National Severe Storms Laboratory, Norman, Oklahoma

JOSEPH C. PICCA

NOAA/NWS/NCEP/Storm Prediction Center, Norman, Oklahoma

(Manuscript received 13 February 2018, in final form 23 July 2018)

ABSTRACT

Raindrop size sorting is a ubiquitous microphysical occurrence in precipitating systems. Owing to the greater terminal fall speed of larger particles, a raindrop's fall trajectory can be sensitive to its size, and strong air currents (e.g., a convective updraft) can enhance this sensitivity. Indeed, observational and numerical model simulation studies have confirmed these effects on raindrop size distributions near convective updrafts. One striking example is the lofting of liquid drops and partially frozen hydrometeors above the environmental 0°C level, resulting in a small columnar region of positive differential reflectivity Z_{DR} in polarimetric radar data, known as the Z_{DR} column. This signature can serve as a proxy for updraft location and strength, offering operational forecasters a tool for monitoring convective trends. Beneath the 0°C level, where WSR-88D spatiotemporal resolution is highest, anomalously high Z_{DR} collocated with lower reflectivity factor at horizontal polarization Z_H is often observed within and beneath convective updrafts. Here, size sorting creates a deficit in small drops, while relatively large drops and melting hydrometeors are present in low concentrations. As such, this unique raindrop size distribution and its related polarimetric signature can indicate updraft location sooner and more frequently than the detection of a Z_{DR} column. This paper introduces a novel algorithm that capitalizes on the improved radar coverage at lower levels and automates the detection of this size sorting signature. At the algorithm core, unique Z_H–Z_{DR} relationships are created for each radar elevation scan, and positive Z_{DR} outliers (often indicative of size sorting) are identified. Algorithm design, examples, performance, strengths and limitations, and future development are discussed.

1. Introduction

The upgrade of the Weather Surveillance Radar-1988 Doppler (WSR-88D) with polarimetric capabilities continues to fuel a resurgence in microphysical studies of precipitating systems. The transmission/reception of orthogonally polarized waves by these radars has provided a wealth of new information regarding the characteristics of hydrometeors within precipitating systems. In turn, forecasters have access to improved radar-based hydrometeor classification (e.g., Park et al. 2009) and quantitative precipitation estimation (e.g., Giangrande and Ryzhkov 2008) algorithms. For a detailed overview and discussion regarding commonly used polarimetric radar variables, including radar reflectivity factor at horizontal polarization Z_H, copolar cross-correlation coefficient ρ_{hv}, specific differential phase K_{DP}, and differential reflectivity Z_{DR}, the reader is referred to Doviak and Zrnić (1993), Bringi and Chandrasekar (2001), and Kumjian (2013a,b,c).

Perhaps more importantly, this new information can highlight microphysical processes that reveal critical details about the evolution of precipitating systems such as thunderstorms. Polarimetric radar data can be used to identify changes in the hydrometeor distribution within various parts of a storm, potentially signaling imminent convective growth or decay. For example, polarimetric

[a] Current affiliation: Cooperative Institute for Research in Environmental Sciences, University of Colorado, and NOAA/OAR/ESRL/Global Systems Division, Boulder, Colorado.

Corresponding author: Darrel Kingfield, darrel.kingfield@noaa.gov

radar can distinguish between drops of different sizes—most notably via Z_{DR} (Seliga and Bringi 1976)—providing the ability to investigate microphysical processes in greater detail. Z_{DR} is proportional to the aspect ratio of hydrometeors that are small relative to the radar wavelength. Moreover, the magnitude of Z_{DR} increases with increasing dielectric constant for a given particle size and shape. However, pure raindrops have a steady dielectric constant, and their axis ratio increases monotonically (i.e., they become more oblate) as their size increases (e.g., Pruppacher and Beard 1970; Brandes et al. 2002). Therefore, operational Z_{DR} data have great utility for analyzing estimates of bulk drop size distributions when used in conjunction with other radar variables.

Owing to their spherical shape, small drops tend to be characterized by Z_{DR} near 0 dB. At S band (WSR-88D wavelength; approximately 10–11 cm), Z_{DR} can increase to near 5 dB for the largest drops (around 8 mm in diameter). For hydrometeors that are large relative to the radar wavelength, Z_{DR} can fluctuate wildly and may no longer be proportional to the hydrometeor aspect ratio, due to resonance scattering (Trömel et al. 2013). In turn, characterizing hydrometeor shape via Z_{DR} is considerably more difficult when resonance scattering is present. However, even the largest raindrops can be considered sufficiently small relative to the radar wavelength when using S-band data. The work presented herein focuses purely on S-band radar data, such that Z_{DR} is utilized heavily to analyze raindrop sizes in a bulk sense.

a. Size sorting

Raindrop size sorting is a ubiquitous feature of precipitating systems. Generally, as raindrops increase in size, so does their terminal fall speed. As a result, raindrops with different sizes can take considerably different trajectories, which are sensitive to the airflow patterns within a precipitating system (Marshall 1953; Gunn and Marshall 1955; Kumjian and Ryzhkov 2012; Dawson et al. 2015). In the simplest form of size sorting, the onset of precipitation occurs when cloud droplets grow large enough to fall toward the ground, while smaller droplets remain suspended. Extending this concept further, large drops reach the surface prior to small drops beneath a nascent precipitating cloud, due to the greater terminal velocity of the large drops. A common anecdote related to such sorting is the initial "splat" of big drops often observed underneath a growing cumuliform cloud. Figure 1 offers an example (via a radar cross section) of this initial differential sedimentation in developing cells.

Such a signature is fairly transient and vanishes once smaller drops begin to reach the surface. In general, this size sorting signature due to initial differential sedimentation lasts no more than 5–10 min, with Z_{DR}

decreasing as more smaller drops contribute to the total backscattered signal at lower-elevation radar scans (Kumjian and Ryzhkov 2012). However, the polarimetric signature of size sorting can be sustained for much longer periods of time via the presence of strong upward motion, such as a convective updraft. Only large drops with terminal velocities exceeding that of the updraft speed descend toward the ground, while smaller drops can be suspended, lifted upward, or detrained from the updraft. The resultant drop size distribution (DSD) at low to midlevels (from the surface to several kilometers aloft) is then skewed toward larger raindrops, with fewer small drops present. Thus, a sustained size sorting signature can serve as a proxy for maturing updraft location, potentially portending near-term cell propagation and intensification. Such information has large implications for the operational convective warning process.

Perhaps the most notable and documented polarimetric signature of updraft-induced size sorting is the Z_{DR} column (e.g., Illingworth et al. 1987; Caylor and Illingworth 1987; Wakimoto and Bringi 1988; Bringi et al. 1991; Conway and Zrnić 1993; Brandes et al. 1995; Jameson et al. 1996; Hubbert et al. 1998; Smith et al. 1999; Kennedy et al. 2001; Loney et al. 2002; Kumjian and Ryzhkov 2008; Kumjian et al. 2012, 2014; Snyder et al. 2015). A Z_{DR} column is the by-product of large drops being lofted by an updraft above the environmental freezing level [see Kumjian et al. (2014) for a summary of the mechanisms driving drop growth]. Stronger updrafts can result in a columnar layer of positive Z_{DR} extending several kilometers beyond the 0°C level (Kumjian and Ryzhkov 2008). As a result, the Z_{DR} column can be used as a proxy for updraft location and perhaps strength (with taller/broader columns potentially suggesting a more robust updraft), making it a favorable tool for convective nowcasting. These signatures are often observed emanating upward from a "foundation" of anomalously high Z_{DR} (for the associated range gate value of Z_H) beneath the 0°C level, which is the lower-level size sorting signature described in the previous paragraph. Figure 2 presents an example of a Z_{DR} column signature extending upward from a zone of high Z_{DR} beneath the 0°C level.

Strong horizontal flow can also sustain size sorting of hydrometeors (Kumjian and Ryzhkov 2012; Dawson et al. 2014). Nonzero storm-relative flow horizontally advects raindrops away from the parent cloud. Since larger drops descend more rapidly than smaller drops, there is less time for downstream advection by the storm-relative wind. Therefore, a stronger storm-relative wind field (over the depth of the sorting layer) will cause a more apparent radar size sorting signature.
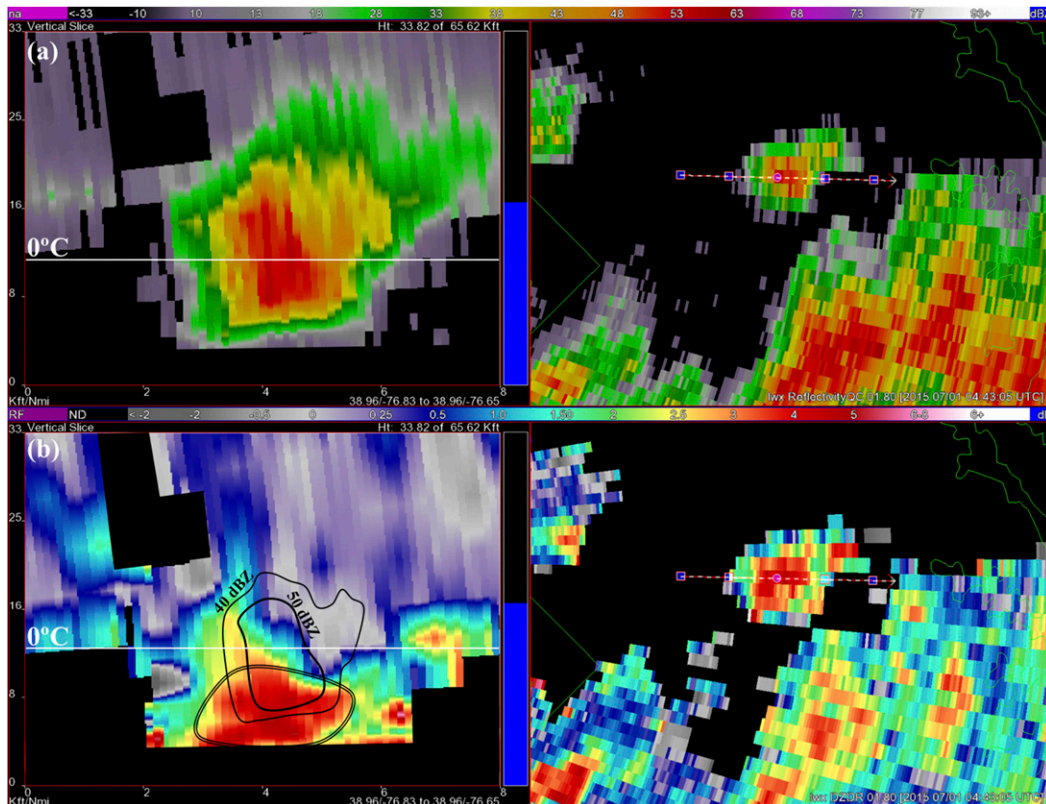
FIG. 1. (left) Cross sections and (right) associated 1.8° elevation scans of (a) Z_H and (b) Z_{DR}. Note the higher values of Z_{DR} annotated in double black lines at the bottom of the developing precipitation core. These values represent initial sedimentation of larger drops—a common size sorting occurrence. The 40- and 50-dBZ contours are overlaid on Z_{DR} for reference.

In the case of a storm-relative wind field that changes direction with height, size sorting may manifest via the Z_{DR} arc signature (Kumjian and Ryzhkov 2009, 2012), which appears on the forward-flank reflectivity gradient along the inflow region of a supercell. Here, the drop size distribution can be characterized by a relatively low number of larger drops (and water-coated ice particles) and a lack of smaller drops (which have been advected farther downstream in the forward-flank region). In turn, the signature is characterized by significant, positive Z_{DR} values (generally greater than 2–3 dB) collocated with low to moderate reflectivity (around 30–40 dBZ or less).

Dawson et al. (2014) found that this signature is related to the mean storm-relative wind vector over the depth of the precipitation shaft above the layer containing the signature. Thus, as the magnitude and shape of the signature are correlated with the strength and direction of the storm-relative wind field, this signature can reveal critical information regarding the near-storm environment—specifically, the likely presence of storm-relative helicity favorable for low-level mesocyclogenesis. While such a capability does not offer explicit prediction of tornadogenesis, it can signal a near-storm environment favorable for tornadogenesis. Robust automated detection of this signature would likely benefit operations considerably.

b. Operational application

Recent numerical simulations incorporating either bin or bulk microphysical schemes have illustrated the diagnostic potential of these polarimetric size sorting signatures (Kumjian and Ryzhkov 2009; Jung et al. 2010; Kumjian and Ryzhkov 2012; Dawson et al. 2014; Kumjian et al. 2014; Dawson et al. 2015; Snyder et al. 2015), highlighting the need for their incorporation into operational radar analysis procedures. Moreover, observational studies have confirmed the operational applicability implied by these simulations. For example, Z_{DR} columns have exhibited a positive lagged correlation with reflectivity-based metrics (e.g., the ratio of the 60-dBZ volume to the 40-dBZ volume; Picca et al. 2010; Kumjian et al. 2014). Such work suggests that ongoing warning operations research should focus on the creation and implementation of
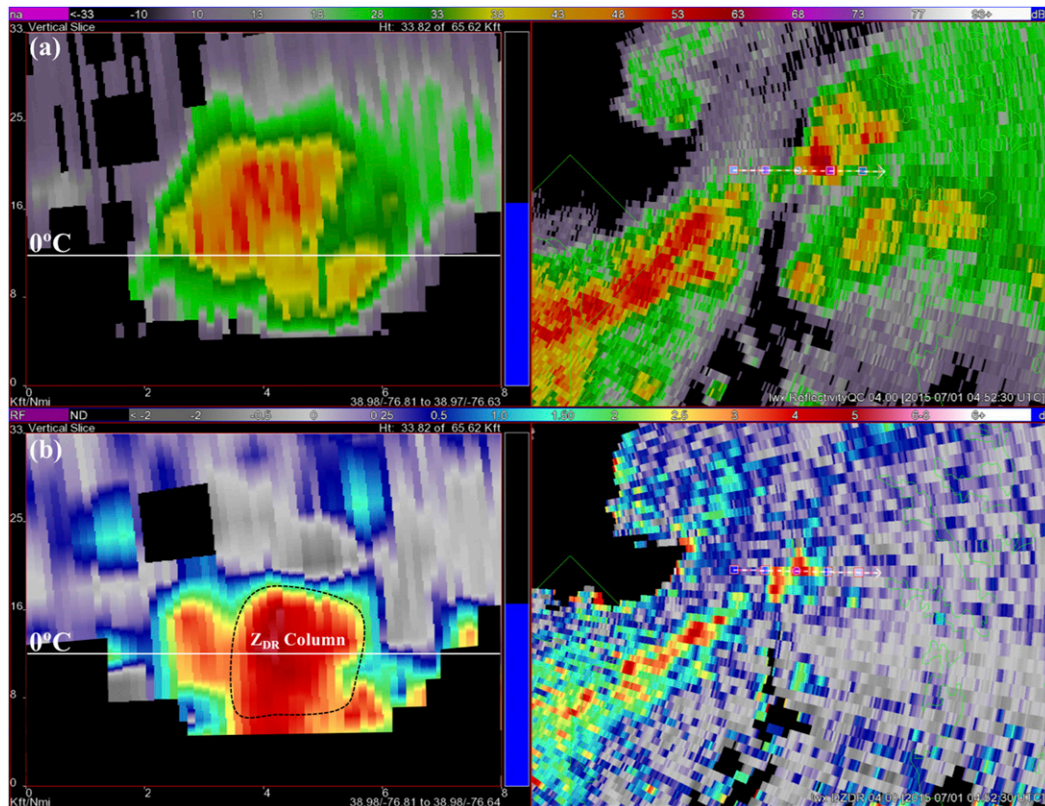
FIG. 2. (left) Cross sections and (right) associated 4.0° elevation scans of (a) Z_H and (b) Z_{DR}. Note the higher values of Z_{DR} extending above the 0°C level represent the Z_{DR} column, which is the result of liquid drops and liquid-coated ice particles lofted by an updraft.

algorithms that capitalize on the microphysical clues offered by polarimetric radar.

Snyder et al. (2015) developed an automated Z_{DR} column algorithm that detects these signatures and outputs a maximum height for each detection, providing a diagnostic tool for assessing updraft evolution. At closer ranges from radar, the algorithm has exhibited skill in assessing updraft strength with more robust, organized cells. Such next-generation radar algorithms can enable more operational meteorologists to utilize the powerful diagnostic capabilities of polarimetric radar. These algorithms lessen the ''data overload'' of several new variables by synthesizing polarimetric data into one clear output—in this instance, a Z_{DR} column height that serves as a proxy for updraft location and strength.

However, at farther distances and with weaker, less organized convection, the zone of lofted drops above the 0°C level becomes small relative to the radar's effective beamwidth, resulting in a backscattered signal that can easily be masked by other hydrometeors in the range bin. Therefore, Z_{DR} columns can become quite subtle or even nonexistent, such that their utility often decreases with more distant and/or shallower convection. Future

work may be able to quantify the decrease in skill via objective verification of Z_{DR} columns across a wide distribution of ranges from radar.

Updraft-related size sorting does not only occur above the 0°C level, as previously described. Raindrop sorting also occurs within and near updrafts at lower elevations. Thus, radar signatures of low-level size sorting can supplement Z_{DR} columns by offering valuable information regarding convective evolution at altitudes where improved spatiotemporal radar coverage typically exists. Figure 3 exhibits the utility of the low-level size sorting signature in terms of nowcasting convective evolution.

Despite this capability, the low-level signature can be more difficult to identify (relative to the Z_{DR} column), as Z_{DR} is generally higher everywhere beneath the melting layer (due to the dominance of liquid scatterers, biota, and so on with intrinsic positive Z_{DR}) than it is above the melting layer. Whereas there is often high contrast between a Z_{DR} column and the ambient background Z_{DR}, the contrast between a low-level size sorting signature and its background Z_{DR} tends to be much lower. Considering the nowcasting utility of this low-level signature, we are motivated to develop an
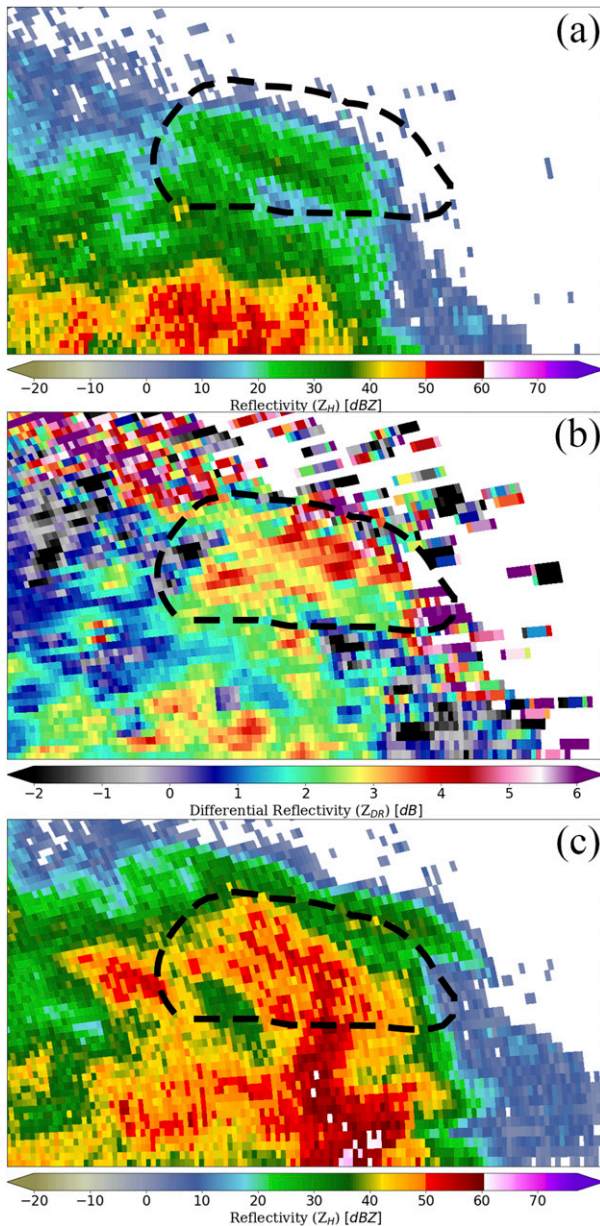
FIG. 3. The 0.5° PPIs from the Goodland, KS (KGLD), radar of (a) Z_H and (b) Z_{DR} at 0133 UTC and (c) Z_H at 0138 UTC 8 Aug 2015. Note the high values of Z_{DR} (>3 dB) associated with Z_H around 25–35 dBZ in (a) and (b). Five minutes later, there is a dramatic increase in Z_H.

algorithm that highlights all zones of hydrometeor size sorting (both low-level and Z_{DR} columns) and provides some quantitative detail regarding the magnitude of sorting. Such an algorithm would likely reduce the analysis load on radar operators while simultaneously enhancing their ability to synthesize polarimetric data with more conventional datasets (e.g., reflectivity, velocity). Subsequently, it would supplement radar operators' ability to nowcast convective evolution.

Paramount to this improvement would be the algorithm's capability to highlight imminent cell propagation and intensification trends (on the order of 0–10 min). Forecasters frequently encounter convective situations in which they must rapidly construct a downstream warning area (e.g., polygon) to alert the public or clients in a timely manner. In turn, a warning forecaster must quickly assess cell evolution and synthesize radar and mesoscale data to predict near-term storm motion. A key component of this motion is cell propagation (e.g., deviant movement in supercells, upshear/downshear MCS propagation), and such trends are not always clear in conventional datasets. With improved visualization of these trends, forecasters could better anticipate overall storm motion and more appropriately tailor the size and shape of short-fused storm-based warnings. Additionally, decision support meteorologists could offer even greater detail on the forecast timing and location of convective impacts.

2. Algorithm overview

The size sorting identification algorithm described in this paper utilizes polarimetric data from operational WSR-88D sites to estimate the magnitude of size sorting via a rapidly updating product (on the order of 2 min), which will be described later in this work. Hereafter, this algorithm is referred to as the Thunderstorm Risk Estimation from Nowcasting Development via Size Sorting (TRENDSS). The TRENDSS algorithm and its preprocessing routines are managed within the Warning Decision Support System–Integrated Information (WDSS–II; Lakshmanan et al. 2007) software framework.

a. Preprocessing

First, Level-II radar data are ingested into WDSS–II to generate Level-III polarimetric data that are equivalent to radar fields produced by the WSR-88D radar product generator. This produces smoothed Z_{DR} and ρ_{hv} fields and estimates the heights of the melting layer top and bottom from the melting layer detection algorithm (MLDA; Giangrande et al. 2008). By smoothing the original Level-II data (from 0.5° to 1° azimuthal resolution via a linear combination), the reduction in variance within these radar fields makes them more suitable for algorithm processing. After this step, the Z_H data are quality controlled using a reflectivity quality control algorithm (Lakshmanan et al. 2007, 2010) to remove returns from nonhydrometeors (e.g., filter clutter, biota). The smoothed Z_{DR}, ρ_{hv}, MLDA, and quality controlled Z_H fields are the four radar inputs into the TRENDSS algorithm. As a backup to the MLDA and to provide the TRENDSS algorithm with a first-guess field of the

TABLE 1. Various thresholds for different radar variables and microphysical layers are presented. Range gates passing these criteria are retained for analysis by the TRENDSS algorithm.

Layer	Reflectivity (dBZ)	Differential reflectivity (dB)	Correlation coefficient
Above melting layer	$\geq$25	<6	$\geq$0.97
Within melting layer	$\geq$25	<6	$\geq$0.98
Below melting layer	$\geq$15	<6	$\geq$0.9

melting level and a ceiling to stop data collection, the environmental 0° and −10°C levels are derived from the 13-km Rapid Refresh (RAP; Benjamin et al. 2016) model, serving as the fifth and final algorithm input.

b. Algorithm core

Fundamentally, the TRENDSS algorithm aims to identify radar gates representative of raindrop size sorting signatures. As previously discussed, such signatures are characterized by Z_{DR} that is anomalously high for the corresponding value of Z_H in a range gate. Thus, some Z_H–Z_{DR} relationship must be constructed to identify anomalously high Z_{DR} values. To do so, TRENDSS first filters range gates that may be dominated by scatterers deemed unsuitable for analysis. Various Z_H, Z_{DR}, and ρ_{hv} thresholds are utilized, with the specific values dependent upon the position of the gate relative to the melting layer (determination of microphysical layers and resultant algorithm "stages" discussed later in this section). Table 1 offers specifics regarding these thresholds.

All thresholds were determined via a heuristic process in which numerous cases from a diverse set of regions and seasons were analyzed (Table 2). For all gates, regardless of height, only Z_{DR} <6 dB is considered suitable for analysis. While Z_{DR} values above this threshold could be associated with meteorological scatterers (and potential size sorting), the possibility of nonmeteorological contamination (insects, birds, etc.) increases considerably with such high values (e.g., Wilson et al. 1994). Below the melting layer, a $\geq$15-dBZ Z_H threshold was chosen to further reduce contamination from biota and other weak returns with potentially questionable data quality. Additionally, a $\geq$0.9 ρ_{hv} threshold was utilized, which serves to filter nonmeteorological scatterers and non-Rayleigh scatterers (e.g., larger melting hailstones), which may have a wildly fluctuating Z_{DR}.

Within and above the melting layer, the Z_H threshold is increased to 25 dBZ to reduce contributions from ice crystals, which can exhibit high Z_{DR} and modest Z_H, yet are not necessarily indicative of storm intensification. The ρ_{hv} threshold is also further tightened within and above the melting layer, where the lower bound increases to 0.98 and 0.97, respectively, to mask ice crystal contamination. The threshold is slightly higher within the melting layer, as isolated gates characterized by very high Z_{DR} (likely composed of initially melting snow) still exhibited ρ_{hv} values around 0.95–0.97 during subjective case analysis. Consistent with ice crystal gates, we do not wish to highlight these gates, owing to the low probability they are associated with size sorting.

There of course remains considerable uncertainty regarding hydrometeor distributions and the corresponding observed polarimetric values within range gates. As such, these filtering values may at times under- or overcensor data; however, prior literature and analysis of TRENDSS output from numerous cases suggests these current values are suitable for operational use. Additionally, future iterations of the algorithm could use dynamic threshold values that more appropriately filter bins unsuitable for analysis. For example, these values could be sensitive to the estimated precipitation regime (e.g., tropical, continental).

With the remaining gates now deemed suitable for processing, TRENDSS approximates up to three Z_H–Z_{DR} relationships for each elevation scan. These three relationships consist of one below the melting layer (stage 1), one within the melting layer (stage 2), and one above the melting layer (stage 3). Radar range gates are classified into one of these stages based upon output from the MLDA with the RAP serving as a backup. These three stages are distinct from one another such that the estimated Z_H–Z_{DR} relationships are at least modestly tailored to the layer being analyzed. For example, Z_{DR} within stage 3 is less likely to increase with increasing Z_H due to the predominance of frozen scatterers. Meanwhile, Z_{DR} typically exhibits a monotonic increase with increasing Z_H in stage 1. Blending data from these stages would result in an estimated relationship that is less representative of the precipitation regimes of all range gates.

At all three stages, we are confident that the majority of TRENDSS detections will be associated with size sorting. The well-established nature of the Z_H–Z_{DR} relationship below the melting layer, combined with the filtering thresholds described above, ensures that low-level detections are very likely from updraft-enhanced sorting, differential sedimentation, or strong storm-relative flow. Our motivation to extend the TRENDSS domain to colder temperatures (i.e., within/above the melting layer) is based in our desire to extend Z_{DR}

TABLE 2. Events analyzed to define the TRENDSS radar parameter thresholds. The four events used to validate the TRENDSS algorithm are marked with an asterisk (*).

Date	Time (UTC)	Region	General storm mode comments
19/20 May 2013	1904–0159	Southern Plains	Discrete supercells
31 May/1 Jun 2013	2201–0055	Southern Plains	Discrete/embedded supercells
29 Apr 2014	1903–2358	Mid-Atlantic	Embedded supercells, bow echoes, multicells
8 Jun 2014	0203–0800	Southern Plains	Supercells, multicells, QLCS with large trailing region
28 Jul 2014	0804–1501	New England	Multicells and bowing segments
13 Aug 2014	0302–1203	Mid-Atlantic	Embedded multicells/line segments
11 Dec 2014	1002–1401	Northern CA	Shallow line segments
24 Dec 2014	1903–2159	OH Valley	Thin QLCS
3 Jan 2015	1803–2158	Lower MS Valley	QLCS and bowing segments
9/10 Apr 2015	2201–0201	Upper Midwest	Discrete/embedded supercells
23/24 May 2015*	1800–0201	Southern Plains	Squall line and supercells
29 May 2015	0204–0901	Southern Plains	QLCS with large trailing region
23 Jun 2015*	2003–2357	Mid-Atlantic	Bow echo
1 Jul 2015	0048–0701	Mid-Atlantic	Multicells and small bowing segments
1 Aug 2015	1600–2100	ME	Supercells and small bowing segments
2 Aug 2015	1704–2257	Upper Midwest	Supercells and bow echoes
6 Aug 2015	1842–2058	NC	Multicells
8 Aug 2015*	0000–0356	Central Plains	Supercells and QLCSs
17/18 Aug 2015	1800–0058	Southeast	Multicells
25 Aug 2015	0703–1056	Northeast	Multicells
30 Aug 2015	2304–0259	AZ	Single cells
3 Sep 2015	1503–1858	MI	Multicells
8 Sep 2015*	1902–2302	Southern CA	Terrain-induced single cells
27/28 Dec 2015	2201–0200	North TX	Supercells and multicells
4 Apr 2016	1900–2301	OK	QLCS and embedded supercells
9/10 May 2016	1906–0104	Southern Plains	Supercells and multicells
16/17 Jun 2016	2005–0004	Mid-Atlantic	Supercells and QLCS

anomalies to the problem of Z_{DR} column identification. Thus, future iterations of the algorithm could potentially predict cell intensification via an integrated height product. For the current iteration, we still retain the three-stage approach. Although this does open the algorithm to false detections from, for example, ice crystals (discussed in further detail in section 4), the filtering thresholds within/above the melting layer are quite strict and were shown to reduce false detections considerably in heuristic testing. Moreover, increasing the domain's vertical coverage increases the likelihood that size sorting will be identified in regions with poor radar coverage and that these identifications will be maintained during smoothing/postprocessing.

Within each stage of each elevation scan, TRENDSS then approximates a unique Z_H–Z_{DR} relationship by creating 5-dB bins (e.g., 15–20, 20–25 dBZ) and calculating the mean μ and standard deviation σ of Z_{DR} within each bin. The mean and standard deviation for a 5-dB bin at each stage for each elevation angle serves as the expected value and the dispersion (or noisiness) of Z_{DR}, respectively. Of note, statistics are not calculated for a particular bin if fewer than 20 sampled range gates are available (due to either low coverage of precipitation and/ or filtering of unsuitable bins). In such instances, expected

Z_{DR} values within stages 1 and 2 are governed by the following equation from Cao et al. (2008):

$$Z_{DR} = 10^{(-2.6857\times10^{-4}Z_H^2 + 0.04892Z_H - 1.4287)},$$

where Z_H and Z_{DR} are expressed in logarithmic scale. This equation was developed from two-dimensional video disdrometer data recorded at different sites in Oklahoma. We chose the equation based on its development from a large dataset collected from all seasons over a 2-yr period (May 2005–May 2007). We acknowledge that a single equation will not accurately capture all precipitation regimes, but it at least offers a basis for continued algorithm operation when data are sparse.

Within stage 3, expected Z_{DR} is set to 0 dB, as most frozen Rayleigh scatterers have intrinsic Z_{DR} near this value. Additionally, for all stages and bins, the default standard deviation is set to 0.5 dB, which was found to be sufficiently representative for most continental convection in our subjective analysis of over 20 cases (Table 2). Indeed, this value differs only slightly from the expected standard deviation of 0.2–0.3 dB theorized by Ryzhkov et al. (2005). Similar to concerns on a singular Z_H–Z_{DR} equation, these values are not optimized for all situations, but in the brief instances of very isolated, developing

convection (in which only a few samples are available), they provide some framework for identifying anomalously high Z_{DR}.

Following the initial relationship approximation, TRENDSS then enters an application step, in which a Z_{DR} anomaly value is calculated for each valid range gate (thresholds in Table 1). This value is simply the difference between the range gate Z_{DR} and the expected Z_{DR}, which is a function of the Z_H bin. TRENDSS normalizes this anomaly by 1σ (also a function of the Z_H bin). For example, the solid line in Fig. 4 represents 3σ above the expected Z_{DR} (the dashed line). Higher values suggest a greater likelihood that the range gate is characterized by ongoing size sorting, potentially signaling the presence of an updraft and/or Z_{DR} arc signature. Thus, this normalized anomaly value is the fundamental output of TRENDSS. Figure 5 is an example of Z_H, Z_{DR}, and resultant normalized anomaly data from one elevation scan.

While there is no clear anomaly threshold that can isolate size sorting gates across an array of precipitation regimes, analysis of over 20 cases (Table 2) across diverse geographic regions, seasons, and precipitating regimes suggests a threshold value around 3σ has the greatest utility in highlighting size sorting gates. To further solidify this conclusion, our objective verification discussion below (section 3) includes analysis of values starting at 1σ.

To minimize false detections (potential causes discussed in section 4), a median filter is implemented on each elevation scan to reduce the presence of noisy data as well as to smooth and emphasize zones of legitimate size sorting. Range gates beyond 20 km from a WSR-88D were smoothed with a three-by-three median filter window (i.e., replacing the central range gate with the median value of its adjacent eight gates). At ranges closer than 20 km where radar gate widths are smaller, the window size is increased to five-by-five (25 total gates) to boost the magnitude of smoothing. This aids in mitigating noisy data and false detections (e.g., initially unfiltered clutter, biota) that are more prevalent closer to the WSR-88D in nonmountainous regions (e.g., Hubbert et al. 2009).

c. Multiradar design

With TRENDSS operating on all elevation angles of a volume scan, the wealth of additional data can be considerably difficult to integrate into established radar analysis and warning-decision processes of various users (National Weather Service offices, TV meteorologists, air traffic control, etc.). Therefore, TRENDSS incorporates data from multiple radars to produce one primary product (discussed below) that can reduce workload on
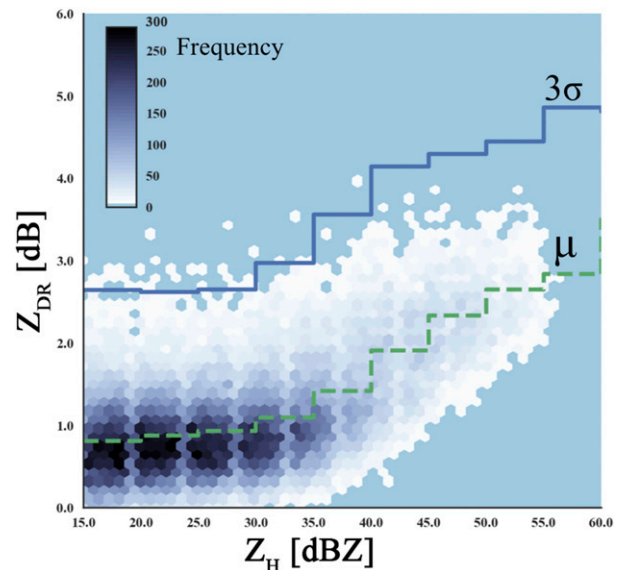

FIG. 4. A hexbin plot representing filtered Z_H and Z_{DR} data from a 5.0° elevation scan by the Sterling, VA (KLWX), radar at 0331 UTC 1 Jul 2015. The frequency of Z_H–Z_{DR} points falling in each hexagon is represented by its corresponding color. The dashed green and solid blue lines indicate the expected/mean Z_{DR} and three standard deviations above the mean, respectively, for each 5-dB bin. Note the points above the blue line—TRENDSS considers these to be size sorting gates.

users. The algorithm core operates uniquely on each elevation scan of every WSR-88D within a specified domain. In this manner, Z_H–Z_{DR} relationship data are not blended among different radars, which would likely hinder the algorithm's ability to identify size sorting. For example, if all Z_H–Z_{DR} pairs are blended into only a few relationships, varying Z_{DR} biases among different radars would produce large standard deviation values (for each Z_H bin), precluding the algorithm from highlighting anomalously high Z_{DR} values. Section 4 expands on TRENDSS's immunity to Z_{DR} miscalibration.

Each valid range gate within the specified domain contains spatial information attributes, such that a three-dimensional volume of Z_{DR} anomaly data is available across the entire domain. For consistency with the approximate volume scan time of a single WSR-88D (when it is operating in a standard convective precipitation mode), TRENDSS maintains data points within this volume if its associated elevation scan timestamp is no more than 5 min old. Thereafter, the data are discarded. Those data within 5 min of the current time are composited onto a Cartesian grid of 0.01° latitude × 0.01° longitude spacing at 2-min intervals. In other words, the maximum value in a vertical column above each grid box is mapped to a single planar view every 2 min. These composited data compose the
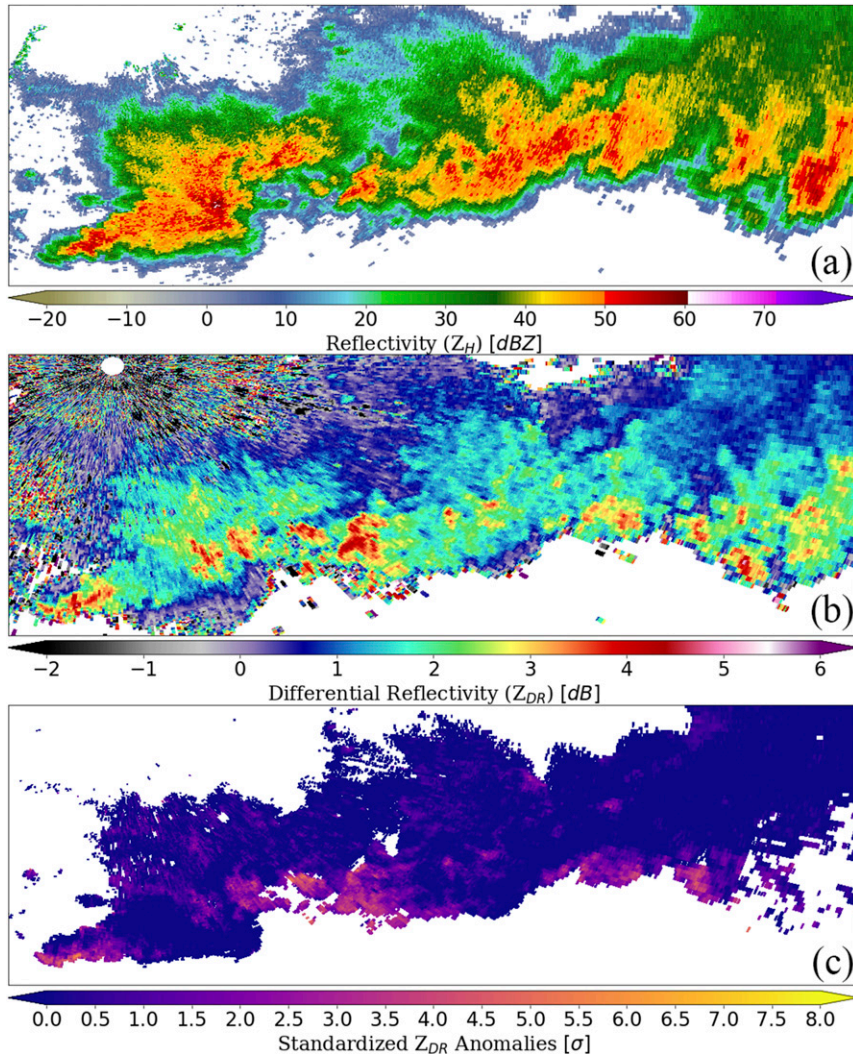
FIG. 5. The 23 Jun 2015 0.5° scans from the Sterling, VA (KLWX), radar of (a) Z_H, (b) Z_{DR}, and (c) standardized Z_{DR} anomalies. Note the higher anomaly values along the leading edge of convection. These are stronger indications of size sorting.

primary TRENDSS product tested below. Figure 6 offers an example of the mosaicked product from 23 June 2015 in the Mid-Atlantic (one of the four cases chosen for objective verification below).

3. Objective verification and case examples

In addition to the subjective analysis performed on cases in Table 2, four cases were chosen for more rigorous objective testing. We selected these cases to test TRENDSS's performance across a diverse range of regions, convective regimes, and cell modes to collect insight regarding the algorithm's ability to predict convective trends on warning/nowcast time scales. Subsequently, this insight can mold best practices for

potential operational implementation within the National Weather Service and other members of the weather enterprise.

We chose the 23 May 2015 southern Great Plains case for its large areal coverage and diverse convective modes. Additionally, the regime was considerably more tropical in nature than is typical for the region, with the 0000 UTC 24 May 2015 Norman, Oklahoma, sounding sampling 44.48 mm of precipitable water. According to SPC sounding climatology (Rogers et al. 2014), this value is the record maximum for the date. The 23 June 2015 Mid-Atlantic case was selected to test a high-impact convective system along the East Coast (NOAA/NCEI 2015), while the 8 August 2015 High Plains case was chosen for both its diversity in convective modes and its
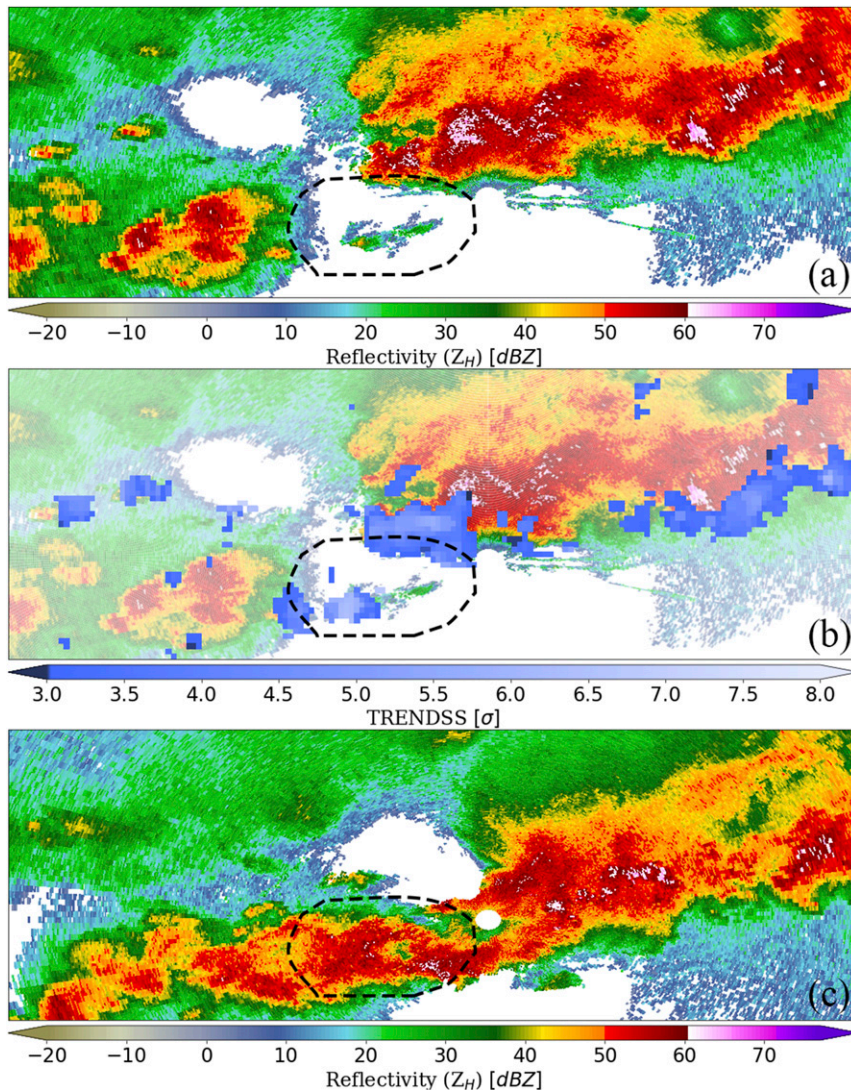
FIG. 6. The 23 Jun 2015 (a) composite reflectivity at 2227 UTC, (b) composite reflectivity and TRENDSS at 2227 UTC, and (c) composite reflectivity at 2248 UTC. Note the TRENDSS identifications near the gap in reflectivity in (b), followed by the expansion of reflectivity in this area shown in (c).

aviation implications—a Delta Air Lines flight encountered a rapidly developing updraft over Nebraska and experienced significant hail damage, necessitating an emergency landing in Denver (NTSB 2015). Last, the 8 September 2015 California case was chosen for its unique geographic region and terrain influence.

For each case, we used the closest hourly 13-km RAP analysis grid to calculate the mean wind field across the cloud-layer depth by averaging the U and V components at all available levels between the lifted condensation level (LCL) and equilibrium level (EL; Fig. 7a). At each 2-min time interval, three sets of TRENDSS objects were identified by region growing (Jain 1989) contiguous

areas starting from a seed grid cell with a minimum TRENDSS value of 1, 2, or 3σ (Fig. 7b). A 10-min forecast plume polygon was created by advecting the TRENDSS object downstream along the mean wind direction vector (Fig. 7c). The Multi-Radar Multi-Sensor (MRMS; Smith et al. 2016) reflectivity at lowest altitude (RALA) product was used to define thunderstorm intensity. It is defined as the closest reflectivity value to Earth's surface that is not terrain blocked and is used by forecasters to diagnose precipitation intensity near the ground. RALA values at $t = 0$ min were collected to quantify the initial state of each plume (Fig. 7d). The final state of each plume was determined by spatially accumulating the maximum RALA
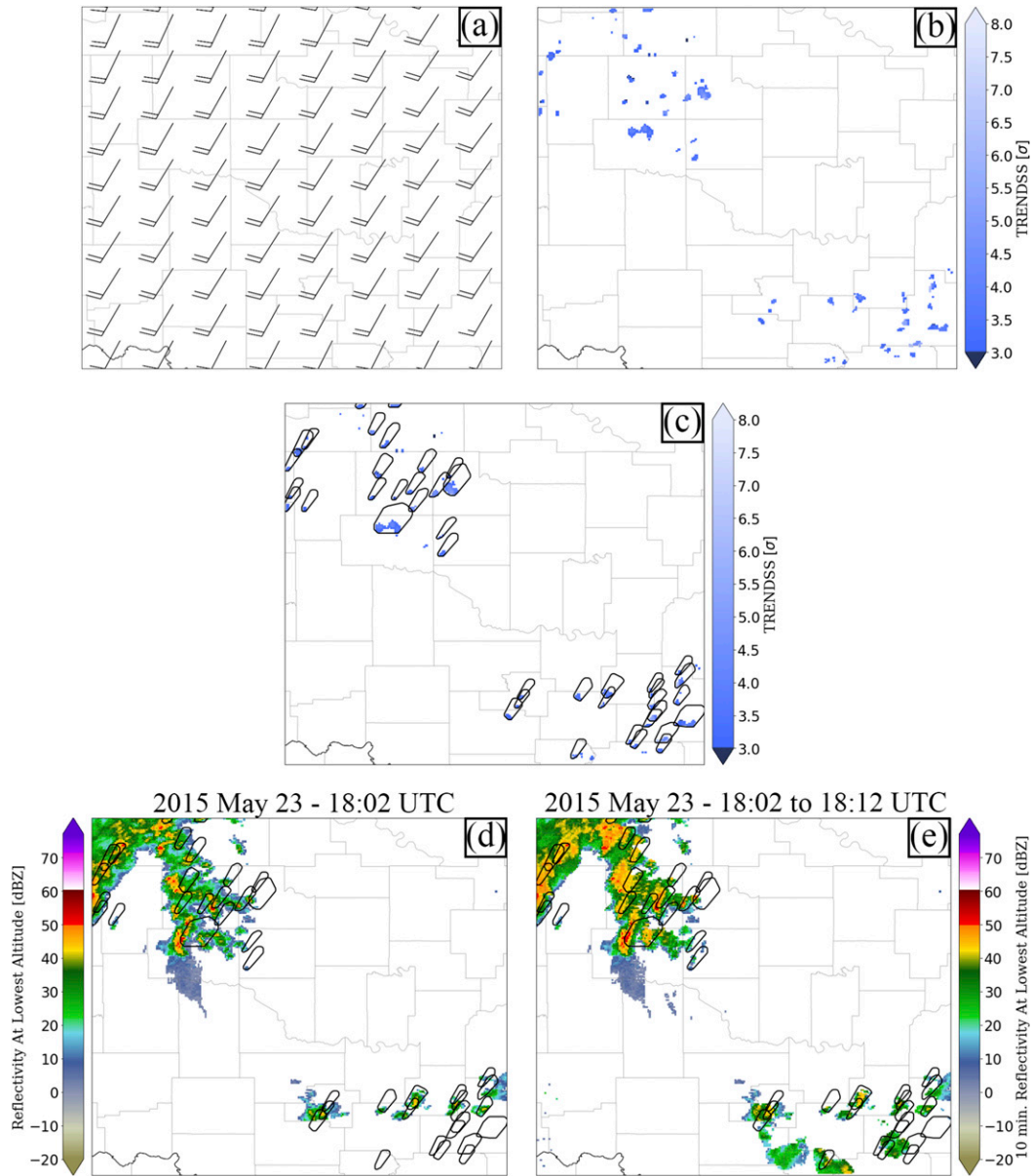
FIG. 7. An automated workflow to verify the TRENDSS algorithm. The (a) mean wind field over the cloud-layer depth and (b) TRENDSS objects exceeding 1, 2, or 3σ (shown here) are used to create 10-min polygons of fore-casted storm location. A comparison of the (d) RALA values at $t = 0$ min to the (e) spatially accumulated RALA values at $t = 10$ min allows for an evaluation of the effectiveness of different TRENDSS sigma levels at nowcasting downstream convective maintenance and intensity.

measured in each grid cell over the next 10 min (Fig. 7e). By comparing these two states, we can quantify the relationship between TRENDSS objects exceeding certain σ thresholds and patterns in convective development.

Objective analysis

Despite being chosen from diverse geographical regions and over a span of several months, TRENDSS objects of at least 3σ exhibited skill in all four cases

tested. These four cases encompassed 32 292 individual cell objects, from which RALA plumes were generated 10 min downstream. In 30 977 of these cases (~95.9% of total), the median RALA within a 10-min plume was equal to or higher than the initial median RALA. Additionally, 16 614 objects (~51.4%) exhibited an increase in median RALA by at least 5 dBZ. Figure 8 displays this bulk signal, suggesting that TRENDSS objects can be a reliable predictor for nowcasting
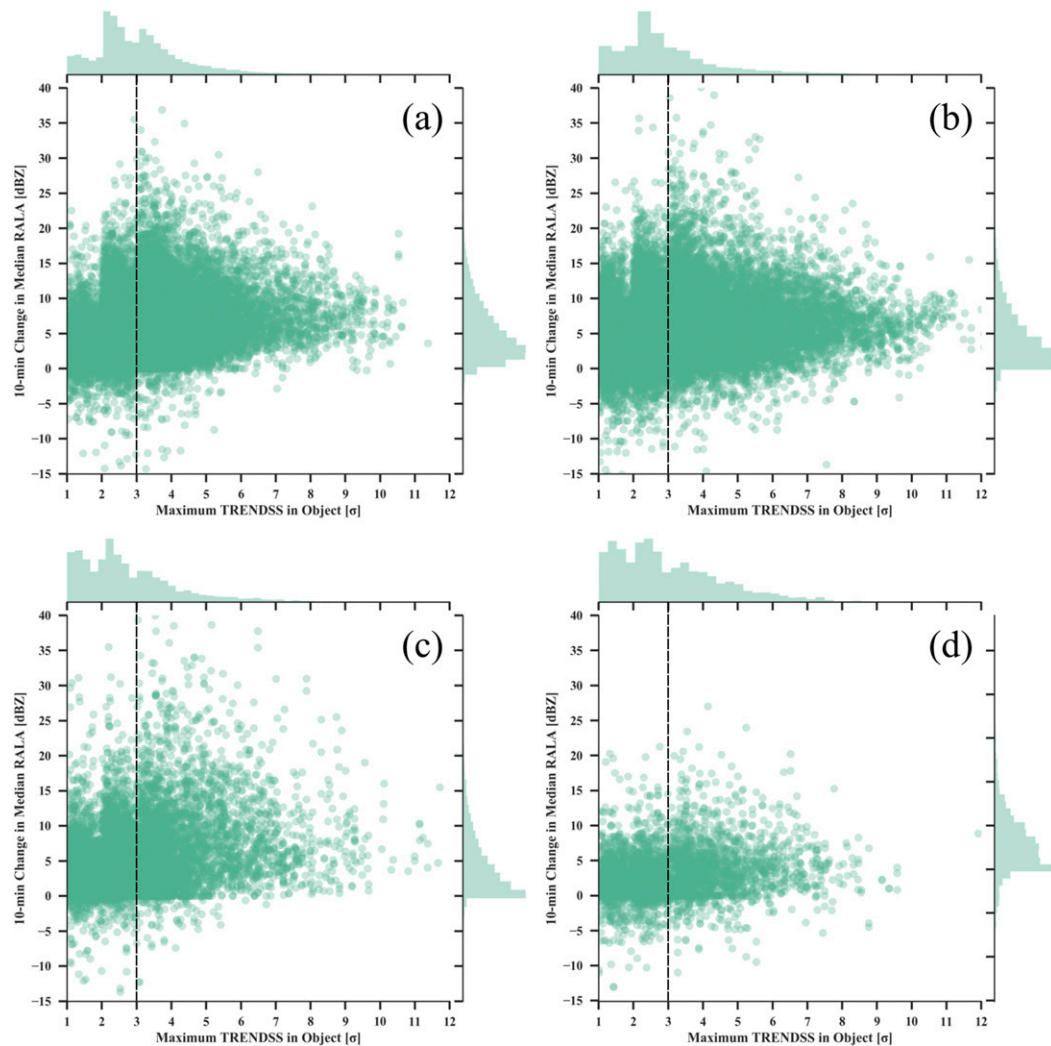
FIG. 8. Scatterplots and related histograms where each data point represents a single TRENDSS object and related downstream plume (characterized by a maximum TRENDSS value and the change in median RALA over 10 min). Points to the right of the dashed black line in each plot correspond to objects with a maximum TRENDSS value exceeding 3σ. The cases are (a) 23/24 May, (b) 23 Jun, (c) 8 Aug, and (d) 8 Sep 2015. For more details on these cases, see Table 2.

downstream maintenance and/or intensification of reflectivity.

Lowering the threshold to 1σ produced an additional 47 904 objects, of which 43 975 (~91.8%) also preceded a change in median RALA of at least 0 dBZ. Initially, these statistics might suggest lowering the threshold to improve algorithm performance. However, only 12 566 of these objects (~26.2%) preceded an increase of at least 5 dBZ. Figure 8 shows clustering of sub-3σ objects around lower values of median RALA difference. Meanwhile, higher values exhibit a slightly greater likelihood of convective maintenance and/or intensification. Therefore, lower-σ objects appear to lack a worthwhile signal for downstream propagation/intensification, especially considering

the large increase in data that forecasters would have to consider if the threshold is lowered.

Of note, the fourth case (Fig. 8d) represents orographically enhanced convection over Southern California. Convective cells and their associated TRENDSS objects remained somewhat sparser than they were with the other three cases, resulting in a reduction of data points and making any relationship between maximum values and reflectivity changes more difficult to ascertain. Furthermore, we acknowledge that changes of approximately 5–10 dBZ do not seem noteworthy; however, considering the large number of objects for each case (on the order of thousands), even a modest increase in median value suggests a consistent signal for intensification.

To further investigate this relationship, maximum TRENDSS values were binned to produce univariate kernel density estimate (KDE) plots of the changes in median RALA value (Fig. 9). The KDE plots utilized a Gaussian kernel and Scott's method (Scott 1992) for determining bandwidth size. In the first three cases (Figs. 9a–c), the peak of each curve moves from near 0 dBZ to approximately 5 dBZ, once again highlighting a modest positive correlation between TRENDSS values and the downstream evolution of reflectivity. Meanwhile, the fourth case (Fig. 9d) exhibits only a very weak relationship, which is likely caused by fewer samples increasing uncertainty with the density estimates, especially at higher maximum TRENDSS values.

Overall, TRENDSS appears to be a reliable identifier of size sorting and the propagation component of storm motion. Our testing methods considered the advection component of storm motion (via the 10-min plume based on mean convective layer wind), such that the addition of the propagation component (via the actual TRENDSS object) offers a robust estimate of total storm motion. Indeed, these results lend confidence in the algorithm's ability to assist in the nowcasting of storm motion. Regarding prediction of cell intensification, our verification methods imply that compositing size sorting identification (in the manner of TRENDSS) possesses some skill in forecasting very near-term strengthening. Nonetheless, future observational/model analyses comparing the estimated magnitude of sorting with updraft velocities are needed to further elucidate this relationship. Furthermore, size sorting from processes other than updrafts, while much less common, will be highlighted by TRENDSS. For example, size sorting within a Z_{DR} arc signature will frequently be identified, and this signature is not indicative of cell propagation/intensification (although it can signal increasing storm-relative helicity, which influences propagation). Benefits of such identification are discussed in section 4.

We acknowledge that uncertainty exists in this analysis, as some cases may be impacted by unrelated convection moving through the downstream plume of the original object. Thus, we constrained the plume to only 10 min downstream, with a buffer of 1 km to focus on very near-term cell propagation. By constraining the plume to 10 min, we also reduce the potential for persistent, deviant propagation to undermine our verification methods. In other words, the 10-min plume is testing propagation predicted by the specific TRENDSS object identified at $t = 0$. A longer plume would likely require more sophisticated object tracking (and more dynamic plume generation) to maintain robust verification methods. While we did not perform such an analysis, future work could investigate the temporal continuity
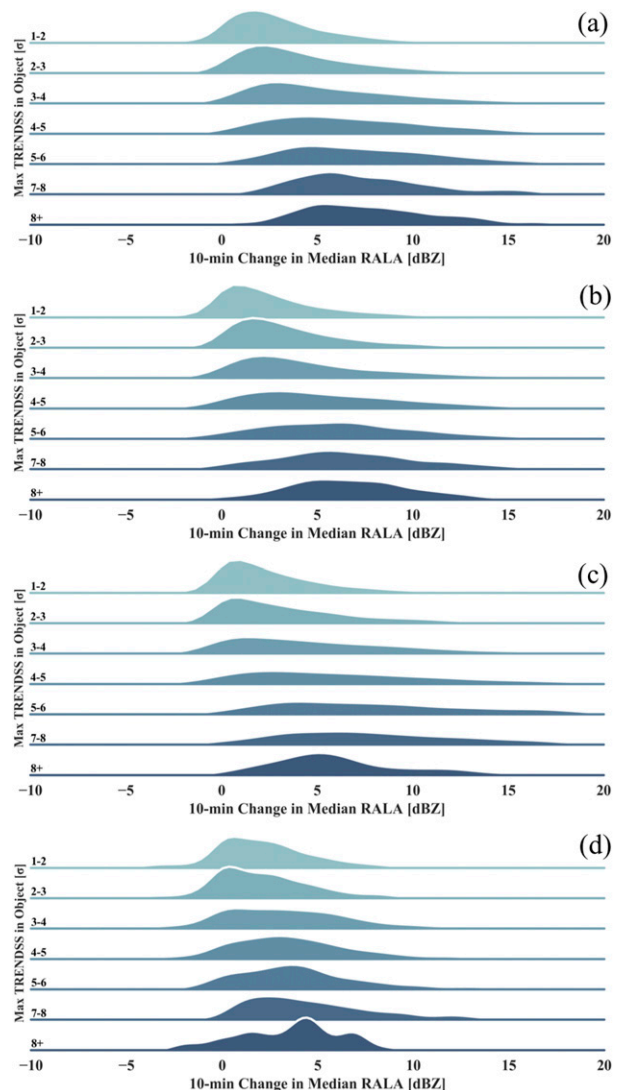

FIG. 9. Kernel density estimates of the 10-min change in median RALA, binned by maximum TRENDSS value, for (a) 23/24 May, (b) 23 Jun, (c) 8 Aug, and (d) 8 Sep 2015. The probabilities range from 0 to approximately 0.15. For more details on these cases, see Table 2.

of TRENDSS objects, perhaps offering new avenues for storm motion prediction. Finally, we aimed to avoid "cherry picking" by automating the identification of TRENDSS objects and downstream plume creation.

Another consideration is that our verification methods do not account for missed events (i.e., we do not identify storms without TRENDSS objects). Although we are certain that some storms do intensify without radar identification of size sorting (e.g., due to masking of sorting gates), our subjective analysis of the cases in Table 2 indicates that cells are not as likely to maintain or increase intensity if their corresponding standardized Z_{DR} anomalies remain below 3σ. However, future

analysis of the performance of TRENDSS should more formally investigate cells that lack size sorting signals.

4. Algorithm strengths and weaknesses

The primary motivation behind TRENDSS is the automated detection of size sorting via the synthesis of three polarimetric fields—Z_H, Z_{DR}, and ρ_{hv}. The goal of this algorithm is to reduce analysis workload on forecasters, while simultaneously leveraging the microphysical information of polarimetric radar for improved near-term prediction of convective trends. We understand that the integration of such automation into established radar analysis routines can prove difficult if an algorithm proves too complex (i.e., difficult to understand) and/or is fraught with conditions or exceptions for its proper use. Therefore, we designed TRENDSS in a manner that minimizes some issues that can plague other algorithms.

a. Strengths

1) IMMUNITY TO Z_{DR} BIAS

While National Weather Service meteorologists and technicians strive to maintain proper Z_{DR} calibration of the WSR-88D fleet, calibration within ± 0.1 dB (the precision required for accurate quantitative precipitation estimation algorithms; Ryzhkov et al. 2005) has proven challenging. Therefore, forecasters and other users occasionally are forced to interpret biased Z_{DR} data, hindering radar analysis during potentially fast-paced warning operations. This drawback must be considered when designing or using an algorithm incorporating Z_{DR} data. A benefit of TRENDSS is its utilization of Z_{DR} anomaly data based on an expected value calculated from local data. By doing so, it incorporates any Z_{DR} bias that may exist, rendering the algorithm immune to miscalibration. For example, if a radar is plagued by a positive 0.5-dB Z_{DR} bias, the expected (mean) Z_{DR} values for each bin will accordingly increase 0.5 dB, and the standardized anomalies will remain unchanged. Therefore, unlike many other polarimetric-based algorithms, TRENDSS data are not degraded by poor Z_{DR} calibration.

2) MOSAICKING/MULTIRADAR DESIGN

Developed within the WDSS–II/MRMS paradigm, TRENDSS incorporates polarimetric data from multiple radars, thereby offering improved spatiotemporal coverage. Moreover, while the viewing angle of one radar may be impacted by differential attenuation or nonuniform beam filling (NBF), another radar may have an unobstructed view of the storm cell of interest. The second radar, thus, can provide meaningful input to the TRENDSS algorithm. Also, during the compositing process, it is unlikely that local TRENDSS data impacted by differential attenuation or NBF from the first radar would mask more accurate data from the second radar. Except in rare instances of anisotropic blockage by trees, towers, and other thin objects, differential attenuation would produce negatively biased radials of Z_{DR} data, leading to negative anomalies in TRENDSS. Because of their negative values, these data points would be overridden by the second radar's data in the compositing process. Meanwhile, gates characterized by excessive NBF (and an attendant reduction of data quality down radial) would likely be filtered by ρ_{hv} thresholds within the initial TRENDSS preprocessing steps. As such, most radar artifacts are unlikely to contaminate or mask legitimate size sorting detections by a second radar.

3) AUTOMATED Z_{DR} ARC DETECTION

Although the original motivation for TRENDSS is based in cell motion prediction, automated Z_{DR} arc identification presents a noteworthy operational opportunity. Manual identification of Z_{DR} arcs within the fast-paced convective warning environment can prove challenging. Therefore, TRENDSS's ability to highlight this feature is a considerable achievement. Figure 10 illustrates this ability with a supercell south of Dallas, Texas, at 2358 UTC 26 December 2015. The algorithm highlights a Z_{DR} arc in Fig. 10c, suggesting the near-storm environment was characterized by ample storm-relative flow (and likely helicity). Three minutes after this radar image, a tornado developed in Midlothian, Texas, eventually producing EF-3 damage (NOAA/NCEI 2015). Although we stress that Z_{DR} arcs do not explicitly predict tornadogenesis, they can signal near-storm environments favorable for stronger low-level mesocyclones, which can increase the probability of tornadogenesis.

b. Weaknesses

1) RADIALS OF NBF OR DIFFERENTIAL ATTENUATION

The algorithm utilizes ρ_{hv} to filter data from melting hydrometeors, diverse ice crystal habits, non-Rayleigh scattering, low signal-to-noise ratio, NBF, and so on. These occurrences can make size sorting detection quite difficult, and thus gates characterized by these features are masked. However, radially oriented zones of low ρ_{hv} due to NBF may mask downstream zones of size sorting if downstream ρ_{hv} is reduced below algorithm thresholds (Table 1). If no other radar data are available, then detection of this size sorting will be impossible. Similarly, differential attenuation can also render downradial detection impossible. Excessive attenuation of power within the horizontal channel will negatively bias
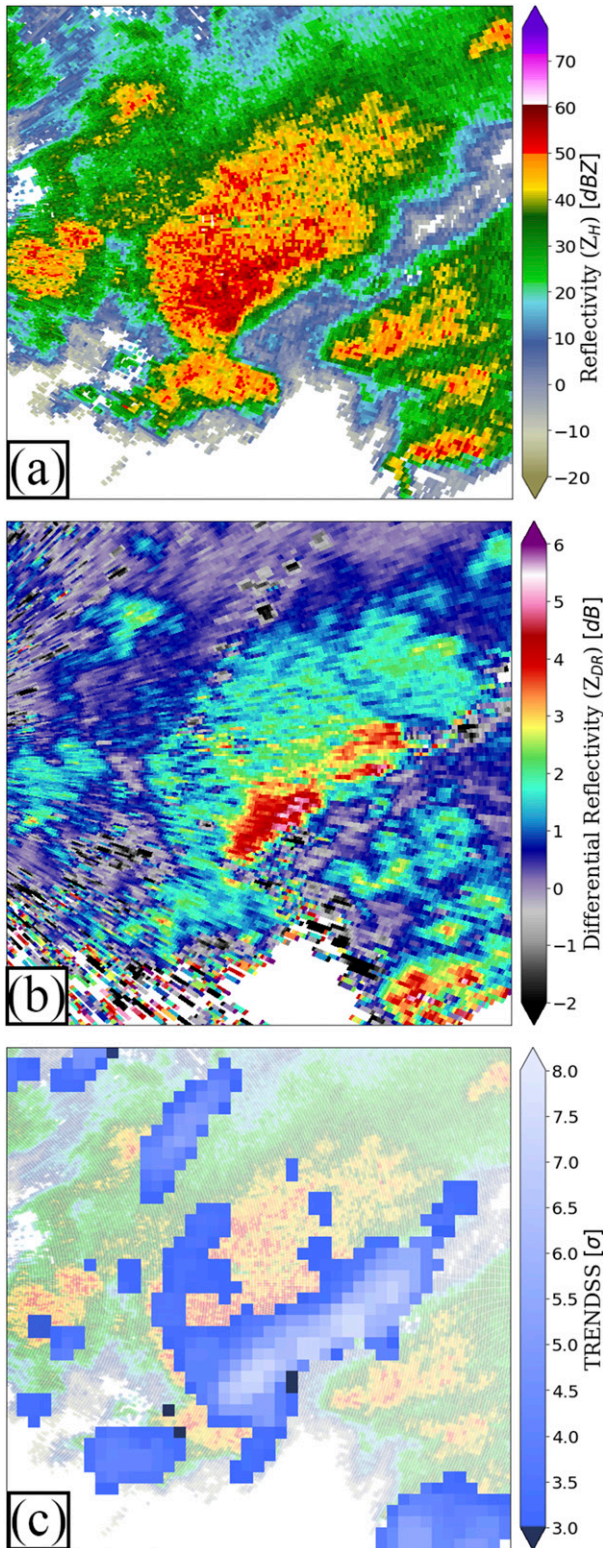
FIG. 10. The 26 Dec 2015 0.5° scans from the Dallas/Fort Worth, TX (KFWS), radar of (a) Z_H, (b) Z_{DR}, and (c) TRENDSS overlaid on Z_H at 2358 UTC for a supercell south of Dallas, TX. The southwest–northeast-oriented corridor of high TRENDSS values along the forward-flank reflectivity gradient of the supercell indicates the presence of a Z_{DR} arc.

Z_{DR} measurements down radial. If the attenuation is great enough, size sorting gates will be represented by Z_{DR} values near/below the expected value from the local relationship, thereby rendering detection of size sorting impossible if there are no additional radar data. In turn, users of TRENDSS data should be aware of the potential for missed identifications in areas of sparse radar coverage. Figure 11a illustrates both differential attenuation and NBF down radial of a heavy precipitation core.

These issues will be magnified for users implementing only a single-radar composite of Z_{DR} anomaly data. At closer ranges, radar analysis benefits from improved spatial resolution and lower potential for gates to be impacted by differential attenuation and/or NBF. With increasing range, single-radar Z_{DR} anomaly data will suffer from the same issues (e.g., beam broadening, increasing altitude) that impact other radar data. Therefore, radar operators should be especially aware of the decreasing performance of single-radar Z_{DR} anomaly algorithms at more distant ranges from radar.

2) ICE CRYSTAL CONTAMINATION

Often, ice crystals exhibit reduced ρ_{hv} and Z_H values, due to their diverse shapes and smaller sizes. Therefore, gates dominated by these scatterers are typically filtered and not passed downstream to the algorithm core. On infrequent occasion, however, the defined filters are not strict enough to remove all range gates dominated by ice crystals. These instances present a challenge, in that pristine crystals can exhibit high Z_{DR} values (due to their oblate alignment during descent), which TRENDSS interprets as anomalously high. In turn, crystals can masquerade as detections of impending convective propagation and/or intensification. Note the TRENDSS identifications along the fringes of stratiform precipitation in Fig. 11b. Analysis of this case suggested little to no convectively enhanced size sorting.

While further tightening of filter thresholds would be an intuitive step to alleviate this issue, testing on cases in Table 2 suggests tightening beyond current thresholds causes excessive masking of legitimate size sorting signatures. Therefore, the current thresholds appear to offer a reasonable compromise to filter as many ice crystal gates as possible, while maintaining legitimate size sorting. Moreover, any remaining contamination is further reduced by median filtering. Any residual false alarms are often transient and relegated to the edges of stratiform precipitation shields, such that they should be relatively easy for a forecaster to identify manually. Users of TRENDSS data should factor in the longevity, magnitude, and relative location of size sorting detections to ensure greater accuracy in near-term prediction of convective trends.
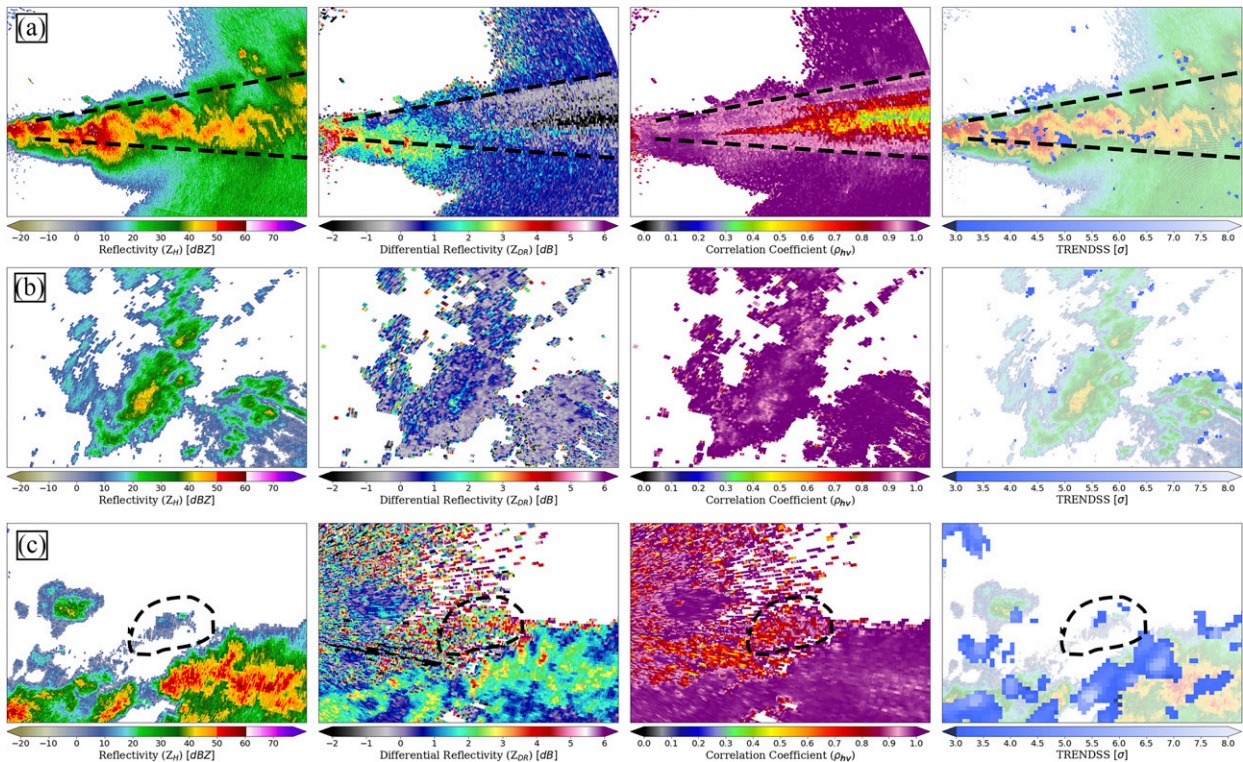
FIG. 11. Examples of radar and meteorological features that can be challenging for the TRENDSS algorithm. This includes (a) nonuniform beam filling (region annotated in black) from the Hastings, NE (KUEX), radar at 0227 UTC 17 Jun 2017, (b) ice crystal contamination from the Upton, NY (KOKX), radar at 1100 UTC 13 Aug 2014, and (c) differential sedimentation (region annotated in black) from the Sterling, VA (KLWX), radar at 0441 UTC 1 Jul 2017.

3) DIFFERENTIAL SEDIMENTATION

In nascent precipitating cells, initial size sorting distributions are a by-product of differential sedimentation, as larger raindrops descend more rapidly than smaller ones do. TRENDSS is designed to capture all size sorting; therefore, differential sedimentation is often identified in new cells. Figure 11c gives an example of such an instance. These cells may not have much potential for intensification, but transient Z_{DR} anomalies over 3σ may be realized for 5–10 min at lower elevations. Nonetheless, if a sustained, vigorous updraft is present, TRENDSS should maintain higher anomalies (both in composite and height) for a longer duration. Therefore, users should place the greatest probability of intensification on cells with persistent, high anomalies (on the order of tens of minutes).

5. Conclusions

Forecast and thunderstorm warning operations are becoming increasingly nuanced in the weather enterprise, owing to a greater focus on decision support services, impacts-based forecasting, and probabilistic warnings

(e.g., Rothfusz et al. 2018). In turn, forecast products must continually leverage the greater detail offered by the latest observational and model data. The TRENDSS algorithm aims to do so by capitalizing on hydrometeor shape information provided by Z_{DR}. By dynamically estimating Z_H–Z_{DR} relationships and identifying areas of anomalously high Z_{DR}, the algorithm can highlight ongoing raindrop size sorting, often portending downstream convective evolution. Moreover, the local nature of the relationships renders the algorithm immune to Z_{DR} miscalibration.

Initial subjective and objective analysis indicates that the algorithm performs reliably in emphasizing areas of new updrafts, related directions of propagation, and potential for near-term intensification. In numerous cases, cells would develop (based on various reflectivity metrics) in the direction of TRENDSS identifications. We believe such information can be useful for warning operations and decision support services by empowering forecasters to make decisions such as the shape of warning polygons with more confidence. Critical to this utility, TRENDSS serves as a new visualization of potential updraft location, which forecasters can use to

diagnose deviant motion, forward acceleration, and so on.

The algorithm is not without needs for future development. While it does attempt to tailor Z_H–Z_{DR} relationships to local data (i.e., unique relationships for each stage on every elevation angle), this method can still combine varying precipitation regimes into one relationship, rendering anomaly detection less effective. Therefore, future iterations of the algorithm could include relationships tailored to various sectors discriminated by precipitation regime, such as using the MRMS surface precipitation type product (Qi et al. 2013; Zhang et al. 2016).

Another target of opportunity is the incorporation of height information into the algorithm. While the current iteration can struggle to differentiate updrafts from Z_{DR} arcs (by compositing data), vertical consistency checks for "columns" of size sorting, similar to the manner of the Z_{DR} column algorithm (Snyder et al. 2015), could output a maximum height of sorting for each grid box. In turn, the algorithm would potentially discriminate between deeper updrafts and lower-level Z_{DR} arc signatures. Moreover, such discrimination would solidify automated Z_{DR} arc detection, further enhancing support for warning forecasters and mesoscale analysts.

More intensive observational and modeling examinations that compare Z_{DR} anomalies and vertical velocity are also needed to establish the robustness of the relationship between TRENDSS and updraft location. Modeling updrafts and their related polarimetric signatures (followed by a TRENDSS-like analysis of the simulated polarimetric field) would offer insight regarding these anomalies and vertical motion, perhaps guiding further refinement of the algorithm. Indeed, a merging of the current technique with a vertical integration such as that of the Z_{DR} column algorithm may yield a comprehensive, automated updraft detection and visualization scheme that could benefit the weather enterprise considerably.

REFERENCES

Benjamin, S. G., and Coauthors, 2016: A North American hourly assimilation and model forecast cycle: The Rapid Refresh. *Mon. Wea. Rev.*, **144**, 1669–1694, https://doi.org/10.1175/MWR-D-15-0242.1.

Brandes, E. A., J. Vivekanandan, J. D. Tuttle, and C. J. Kessinger, 1995: A study of thunderstorm microphysics with multiparameter radar and aircraft observations. *Mon. Wea. Rev.*, **123**, 3129–3143, https://doi.org/10.1175/1520-0493(1995)123<3129:ASOTMW>2.0.CO;2.

——, G. Zhang, and J. Vivekanandan, 2002: Experiments in rainfall estimation with a polarimetric radar in a subtropical environment. *J. Appl. Meteor.*, **41**, 674–685, https://doi.org/10.1175/1520-0450(2002)041<0674:EIREWA>2.0.CO;2.

Bringi, V. N., and V. Chandrasekar, 2001: *Polarimetric Doppler Weather Radar.* 1st ed. Cambridge University Press, 636 pp.

——, D. A. Burrows, and S. M. Menon, 1991: Multiparameter radar and aircraft study of raindrop spectral evolution in warm-based clouds. *J. Appl. Meteor.*, **30**, 853–880, https://doi.org/10.1175/1520-0450(1991)030<0853:MRAASO>2.0.CO;2.

Cao, Q., G. Zhang, E. Brandes, T. Schuur, A. Ryzhkov, and K. Ikeda, 2008: Analysis of video disdrometer and polarimetric radar data to characterize rain microphysics in Oklahoma. *J. Appl. Meteor. Climatol.*, **47**, 2238–2255, https://doi.org/10.1175/2008JAMC1732.1.

Caylor, I. J., and A. J. Illingworth, 1987: Radar observations and modelling of warm rain initiation. *Quart. J. Roy. Meteor. Soc.*, **113**, 1171–1191, https://doi.org/10.1002/qj.49711347806.

Conway, J. W., and D. S. Zrnić, 1993: A study of embryo production and hail growth using dual-Doppler and multiparameter radars. *Mon. Wea. Rev.*, **121**, 2511–2528, https://doi.org/10.1175/1520-0493(1993)121<2511:ASOEPA>2.0.CO;2.

Dawson, D. T., E. R. Mansell, Y. Jung, L. J. Wicker, M. R. Kumjian, and M. Xue, 2014: Low-level Z_{DR} signatures in supercell forward flanks: The role of size sorting and melting of hail. *J. Atmos. Sci.*, **71**, 276–299, https://doi.org/10.1175/JAS-D-13-0118.1.

——, ——, and M. R. Kumjian, 2015: Does wind shear cause hydrometeor size sorting? *J. Atmos. Sci.*, **72**, 340–348, https://doi.org/10.1175/JAS-D-14-0084.1.

Doviak, R. J., and D. S. Zrnić, 1993: *Doppler Radar and Weather Observations.* 2nd ed. Academic Press, 562 pp.

Giangrande, S. E., and A. V. Ryzhkov, 2008: Estimation of rainfall based on the results of polarimetric echo classification. *J. Appl. Meteor. Climatol*, **47**, 2445–2462, https://doi.org/10.1175/2008JAMC1753.1.

——, J. M. Krause, and A. V. Ryzhkov, 2008: Automatic designation of the melting layer with a polarimetric prototype of the WSR-88D radar. *J. Appl. Meteor. Climatol.*, **47**, 1354–1364, https://doi.org/10.1175/2007JAMC1634.1.

Gunn, K. L. S., and J. S. Marshall, 1955: The effect of wind shear on falling precipitation. *J. Meteor.*, **12**, 339–349, https://doi.org/10.1175/1520-0469(1955)012<0339:TEOWSO>2.0.CO;2.

Hubbert, J. C., V. N. Bringi, L. D. Carey, and S. Bolen, 1998: CSU-CHILL polarimetric radar measurements from a severe hail

storm in eastern Colorado. *J. Appl. Meteor.*, **37**, 749–775, https://doi.org/10.1175/1520-0450(1998)037<0749:CCPRMF>2.0.CO;2.

——, M. Dixon, S. M. Ellis, and G. Meymaris, 2009: Weather radar ground clutter. Part I: Identification, modeling, and simulation. *J. Atmos. Oceanic Technol.*, **26**, 1165–1180, https://doi.org/10.1175/2009JTECHA1159.1.

Illingworth, A. J., J. W. F. Goddard, and S. M. Cherry, 1987: Polarization radar studies of precipitation development in convective storms. *Quart. J. Roy. Meteor. Soc.*, **113**, 469–489, https://doi.org/10.1002/qj.49711347604.

Jain, A., 1989: *Fundamentals of Digital Image Processing.* Prentice Hall, 569 pp.

Jameson, A. R., M. J. Murphy, and E. P. Krider, 1996: Multiple-parameter radar observations of isolated Florida thunderstorms during the onset of electrification. *J. Appl. Meteor.*, **35**, 343–354, https://doi.org/10.1175/1520-0450(1996)035<0343:MPROOI>2.0.CO;2.

Jung, Y., M. Xue, and G. Zhang, 2010: Simulations of polarimetric radar signatures of a supercell storm using a two-moment bulk microphysics scheme. *J. Appl. Meteor. Climatol.*, **49**, 146–163, https://doi.org/10.1175/2009JAMC2178.1.

Kennedy, P. C., S. A. Rutledge, W. A. Petersen, and V. N. Bringi, 2001: Polarimetric radar observations of hail formation. *J. Appl. Meteor.*, **40**, 1347–1366, https://doi.org/10.1175/1520-0450(2001)040<1347:PROOHF>2.0.CO;2.

Kumjian, M. R., 2013a: Principles and applications of dual-polarization weather radar. Part I: Description of the polarimetric radar variables. *J. Oper. Meteor.*, **1**, 226–242, https://doi.org/10.15191/nwajom.2013.0119.

——, 2013b: Principles and applications of dual-polarization weather radar. Part II: Warm- and cold-season applications. *J. Oper. Meteor.*, **1**, 243–264, https://doi.org/10.15191/nwajom.2013.0120.

——, 2013c: Principles and applications of dual-polarization weather radar. Part III: Artifacts. *J. Oper. Meteor.*, **1**, 265–274, https://doi.org/10.15191/nwajom.2013.0121.

——, and A. V. Ryzhkov, 2008: Polarimetric signatures in supercell thunderstorms. *J. Appl. Meteor. Climatol.*, **47**, 1940–1961, https://doi.org/10.1175/2007JAMC1874.1.

——, and ——, 2009: Storm-relative helicity revealed from polarimetric radar measurements. *J. Atmos. Sci.*, **66**, 667–685, https://doi.org/10.1175/2008JAS2815.1.

——, and ——, 2012: The impact of size sorting on the polarimetric radar variables. *J. Atmos. Sci.*, **69**, 2042–2060, https://doi.org/10.1175/JAS-D-11-0125.1.

——, S. M. Ganson, and A. V. Ryzhkov, 2012: Freezing of raindrops in deep convective updrafts: A microphysical and polarimetric model. *J. Atmos. Sci.*, **69**, 3471–3490, https://doi.org/10.1175/JAS-D-12-067.1.

——, A. P. Khain, N. Benmoshe, E. Ilotoviz, A. V. Ryzhkov, and V. T. Phillips, 2014: The anatomy and physics of Z_{DR} columns: Investigating a polarimetric radar signature with a spectral bin microphysical model. *J. Appl. Meteor. Climatol.*, **53**, 1820–1843, https://doi.org/10.1175/JAMC-D-13-0354.1.

Lakshmanan, V., T. Smith, G. J. Stumpf, and K. Hondl, 2007: The Warning Decision Support System–Integrated Information. *Wea. Forecasting*, **22**, 596–612, https://doi.org/10.1175/WAF1009.1.

——, J. Zhang, and K. Howard, 2010: A technique to censor biological echoes in radar reflectivity data. *J. Appl. Meteor. Climatol.*, **49**, 435–462, https://doi.org/10.1175/2009JAMC2255.1.

Loney, M. L., D. S. Zrnić, J. M. Straka, and A. V. Ryzhkov, 2002: Enhanced polarimetric radar signatures above the melting level in a supercell storm. *J. Appl. Meteor.*, **41**, 1179–1194, https://doi.org/10.1175/1520-0450(2002)041<1179:EPRSAT>2.0.CO;2.

Marshall, J. S., 1953: Precipitation trajectories and patterns. *J. Meteor.*, **10**, 25–29, https://doi.org/10.1175/1520-0469(1953)010<0025:PTAP>2.0.CO;2.

NOAA/NCEI, 2015: Storm Events Database. NOAA/NCEI, https://www.ncdc.noaa.gov/stormevents/.

NTSB, 2015: Delta Air Lines 1889 final report. National Transportation Safety Board Rep. OPS15IA020, https://www.ntsb.gov/_layouts/ntsb.aviation/brief.aspx?ev_id=20150811X22104.

Park, H. S., A. V. Ryzhkov, D. S. Zrnić, and K. Kim, 2009: The hydrometeor classification algorithm for the polarimetric WSR-88D: Description and application to an MCS. *Wea. Forecasting*, **24**, 730–748, https://doi.org/10.1175/2008WAF2222205.1.

Picca, J. C., M. R. Kumjian, and A. V. Ryzhkov, 2010: Z_{DR} columns as a predictive tool for hail growth and storm evolution. *25th Conf. on Severe Local Storms*, Denver, CO, Amer. Meteor. Soc., 11.3, https://ams.confex.com/ams/25SLS/webprogram/Paper175750.html.

Pruppacher, H. R., and K. V. Beard, 1970: A wind tunnel investigation of the internal circulation and shape of water drops falling at terminal velocity in air. *Quart. J. Roy. Meteor. Soc.*, **96**, 247–256, https://doi.org/10.1002/qj.49709640807.

Qi, Y., J. Zhang, and P. Zhang, 2013: A real-time automated convective and stratiform precipitation segregation algorithm in native radar coordinates. *Quart. J. Roy. Meteor. Soc.*, **139**, 2233–2240, https://doi.org/10.1002/qj.2095.

Rogers, J. W., R. L. Thompson, and P. T. Marsh, 2014: Potential applications of a CONUS sounding climatology developed at the Storm Prediction Center. *27th Conf. on Severe Local Storms*, Madison, WI, Amer. Meteor. Soc., 145, https://ams.confex.com/ams/27SLS/webprogram/Paper255385.html.

Rothfusz, L. P., R. Schneider, D. Novak, K. Klockow, A. E. Gerard, C. Karstens, G. J. Stumpf, and T. M. Smith, 2018: FACETs: A proposed next-generation paradigm for high-impact weather forecasting. *Bull. Amer. Meteor. Soc.*, https://doi.org/10.1175/BAMS-D-16-0100.1, in press.

Ryzhkov, A. V., S. E. Giangrande, V. M. Melnikov, and T. J. Schuur, 2005: Calibration issues of dual-polarization radar measurements. *J. Atmos. Oceanic Technol.*, **22**, 1138–1155, https://doi.org/10.1175/JTECH1772.1.

Scott, D. W., 1992: *Multivariate Density Estimation: Theory, Practice, and Visualization.* John Wiley & Sons, 317 pp.

Seliga, T. A., and V. N. Bringi, 1976: Potential use of radar different reflectivity measurements at orthogonal polarizations for measuring precipitation. *J. Appl. Meteor.*, **15**, 69–76, https://doi.org/10.1175/1520-0450(1976)015<0069:PUORDR>2.0.CO;2.

Smith, P. L., D. J. Musil, A. G. Detwiler, and R. Ramachandran, 1999: Observations of mixed-phase precipitation within a CAPE thunderstorm. *J. Appl. Meteor.*, **38**, 145–155, https://doi.org/10.1175/1520-0450(1999)038<0145:OOMPPW>2.0.CO;2.

Smith, T. M., and Coauthors, 2016: Multi-Radar Multi-Sensor (MRMS) severe weather and aviation products: Initial operating capabilities. *Bull. Amer. Meteor. Soc.*, **97**, 1617–1630, https://doi.org/10.1175/BAMS-D-14-00173.1.

Snyder, J. C., A. V. Ryzhkov, M. R. Kumjian, A. P. Khain, and J. C. Picca, 2015: A Z_{DR} column detection algorithm to examine

convective storm updrafts. *Wea. Forecasting*, **30**, 1819–1844, https://doi.org/10.1175/WAF-D-15-0068.1.

Trömel, S., M. R. Kumjian, A. V. Ryzhkov, C. Simmer, and M. Diederich, 2013: Backscatter differential phase—Estimation and variability. *J. Appl. Meteor. Climatol.*, **52**, 2529–2548, https://doi.org/10.1175/JAMC-D-13-0124.1.

Wakimoto, R. M., and V. N. Bringi, 1988: Dual-polarization observations of microbursts associated with intense convection: The 20 July storm during the MIST project. *Mon. Wea. Rev.*, **116**, 1521–1539, https://doi.org/10.1175/1520-0493(1988)116<1521:DPOOMA>2.0.CO;2.

Wilson, J. W., T. M. Weckwerth, J. Vivekanandan, R. M. Wakimoto, and R. W. Russell, 1994: Boundary layer clear-air radar echoes: Origin of echoes and accuracy of derived winds. *J. Atmos. Oceanic Technol.*, **11**, 1184–1206, https://doi.org/10.1175/1520-0426(1994)011<1184:BLCARE>2.0.CO;2.

Zhang, J., and Coauthors, 2016: Multi-Radar Multi-Sensor (MRMS) quantitative precipitation estimation: Initial operating capabilities. *Bull. Amer. Meteor. Soc.*, **97**, 621–638, https://doi.org/10.1175/BAMS-D-14-00174.1.